Influence of crystallographic facet orientations of sol-gel ZnO on the photocatalytic degradation of p-nitrophenol in water

Antoine Farcy [1*], Stéphanie D. Lambert [1], Dirk Poelman [2], Zetian Yang [2], Fabien Drault [3], Sophie Hermans [3], Patrick Drogui [4], Benoît Heinrichs [1], Cédric Malherbe [5], Gauthier Eppe [5], Alexandre Verdin [5], Julien G. Mahy [1,4*]

[1] Department of Chemical Engineering – Nanomaterials, Catalysis & Electrochemistry, University of Liège, B6a, Quartier Agora, Allée du six Août 11, 4000 Liège, Belgium

[2] LumiLab, Department of Solid State Sciences, Ghent University, Krijgslaan 281-S1, Ghent B-9000, Belgium

[3] Institute of Condensed Matter and Nanosciences - Molecular Chemistry, Materials and Catalysis (IMCN/MOST), Université catholique de Louvain, Place Louis Pasteur 1, Box L4.01.03, 1348 Louvain-La-Neuve, Belgium

[4] Institut National de la Recherche Scientifique (INRS), Centre-Eau Terre Environnement, Université du Québec, 490, Rue de la Couronne, Québec (QC), G1K 9A9, Canada

[5] Laboratory of Inorganic Analytical Chemistry, MolSys Research Unit, University of Liege (ULiege), Building B6c, 4000 Liège, Belgium

*Corresponding author: Antoine Farcy; email: antoine.farcy@uliege.be, Julien G. Mahy; email: julien.mahy@uliege.be ; address: Allée du Six Août 11, 4000 Liège, Belgium

Abstract

Three zinc oxide catalysts with different morphologies are synthesized by the sol-gel method. Zinc acetate and hexamethylenetetramine (HMTA) are used to produce nanorods (NR) and nanodiscs (ND). ZnO nanoflowers (NF) are produced from different reactants, namely zinc nitrate and sodium

hydroxide. The photocatalysts are efficient for degrading p-nitrophenol under halogen lamp illumination (300 nm – 800 nm). X-ray diffraction confirms the presence of the wurtzite structure and scanning electron microscopy confirms the desired morphologies. In order to understand the differences in the kinetic rate of degradation between the three catalysts, surface defects are investigated using photoluminescence and Raman spectroscopy. Moreover, colloidal stability and specific surface area are determined by zeta potential and nitrogen sorption measurements, respectively, and allow the impact of the different parameters on the photocatalytic performance of the samples to be clearly understood. Although they do not have the highest number of defects nor the largest specific surface area, ND show the best degradation results by reaching 77% of degradation after 8 h. This result can be attributed to the morphology of this catalyst, where the polar facets are exposed to the medium and play a crucial role in the photocatalytic performance by enhancing the lifetime of the electron/hole pairs generated upon illumination. The polar nature of both catalyst and pollutant increases the contact between them and, consequently, the degradation efficiency.

Keywords: zinc oxide, photocatalysts, morphologies, polar facets, sol-gel, water treatment

1. Introduction

Industrial activity, from its beginning in the 18th century to the present day, has continued to grow in order to meet the demands of society, bringing with it new problems that need to be resolved. Among these, water pollution represents one major nuisance [1]. As water is a natural resource that is essential for all human activities, water disinfection and treatment must be put in place to guarantee its quality. Conventional water disinfection methods such as filtration or chlorination are effective in reducing certain pathogens in water but have limitations when degrading organic pollutants such as pesticides, pharmaceuticals, etc. [2]

The need to develop more efficient chemical methods has led to a growing interest in exploring new advanced oxidation processes (AOP) [3]. AOP consist of the production of highly reactive chemical species, usually hydroxyl radicals, to degrade organic molecules. There are various ways to produce these radicals: homogeneous and heterogeneous photocatalysis [4, 5], ozonation [6], or reactions using Fenton reagents [7]. Among these methods, heterogeneous photocatalysis is a first choice because of its efficiency in degrading a large range of organic pollutants in the water medium, its simple implementation, and their low production cost [8]. Among the possible photocatalysts, zinc oxide (ZnO) has attracted attention for several years. Indeed, it is easy to produce, non-toxic, with a bandgap of 3.3 eV and moreover with a high antibacterial efficiency, which makes it a good candidate for photocatalysis [9].

Governing its activity, among the materials parameters that can be controlled, two appear particularly interesting: the control of the ZnO morphology and the concentration of defects present on the surface of the catalyst [10]. Indeed, as zinc oxide crystallizes with preferential orientations, the synthesis conditions make it possible to control its morphology and study its impact on the catalytic performance [10]. In this sense, the exposed polar and non-polar crystallographic planes seem to play an important role, as well as the type and quantity of defects present on the catalyst surface [11].

Among the different ways to synthesize zinc oxide i.e., hydrothermal [12], solvothermal [13], microwave [14], or sol-gel [15], the sol-gel method presents the advantage of being low-energy and therefore environmentally friendly [15–17]. The photocatalysts presented here will therefore be synthesized by this method.

In this paper, three types of ZnO particles with very different morphologies are studied: nanorods (NR), nanodiscs (ND) and nanoflowers (NF). The influence of different crystallographic planes on the photocatalytic efficiency will be discussed. The diffractograms of these catalysts will be studied to confirm the presence of the wurtzite phase of ZnO in all three cases. Nitrogen sorption is used to determine the BET specific surface area of the samples. Photoluminescence and Raman spectroscopy methods are used to probe the defects present on the surface of the catalysts. Also, diffuse reflectance spectroscopy allows the bandgap energy of the three powders to be determined. The colloidal stability, by determination of the zeta potential, will also be investigated. Finally, a model pollutant will be used: *p*-nitrophenol, in order to study the pollutant degradation kinetics obtained with the synthesized catalysts as a function of all the parameters mentioned above. Our aim is to explore the impact of these parameters on the photocatalytic efficiency.

2. Materials and methods

2.1.Synthesis of photocatalysts with different morphologies

2.1.1. ZnO Nanorods

Zinc acetate (3.0 g) (99%, $Zn(CH_3COO)_2.2H_2O$, VWR CHEMICALS, The Netherlands) and 1.92 g of hexamethylentetramine (99%, SIGMA-ALDRICH, Germany) are added to 360 mL of milli-Q water under stirring. The solution is heated up to 90 °C for 12 h. The resultant powder is washed with water and ethanol before being put in an oven under static air at 100 °C overnight. The resulting ZnO sample is called NR.

2.1.2. ZnO Nanodiscs

The same procedure as described in section 2.1.1 is used to synthesize the ZnO nanodiscs but instead of using 360 mL, 25 mL of water is used to dissolve the precursors. The resulting ZnO sample is called ND.

2.1.3. ZnO Nanoflowers

Zinc nitrate (2.6 g) (98%, $Zn(NO_3)_2.6H_2O$, HONEYWELL, Germany) is dissolved in water (150 mL) under stirring. After complete dissolution of zinc nitrate, an aqueous solution of 0.75 M NaOH (97%, SIGMA-ALDRICH, Germany) is added quickly to the solution until pH 12 is reached. The reaction takes place for 2 h at room temperature. Subsequently, the resulting powder is washed several times with water and ethanol and put in an oven at 80 °C overnight. The resulting ZnO sample is called NF [12] [18].

2.2. Characterization

The microcrystalline structure and phases were determined using a Bruker D8 twin-twin X-ray diffractometer using 1.54 Å (Cu-Kα) radiation in the 2-theta range from 10° to 70°.

Nitrogen adsorption-desorption isotherms were collected on a Micromeritics ASAP 2420 at a temperature of –196 °C. Prior to this, the samples were degassed under high vacuum at 80 °C for 15 h. The specific surface area (S_{BET}) was determined using the Brunauer, Emmett and Teller (BET) equation by obtaining relative pressure data between 0.05 and 0.25.

The morphologies of the three powders were obtained by scanning electron microscopy (SEM) on a TESCAN CLARA device from Bruker operating at 15 kV. The samples, previously dispersed in acetone in an ultrasonic bath for 2 min, were placed on a glass slide divided into eight parts. The latter was metallized with gold before SEM imaging to prevent charging effects.

Photoluminescence emission (PL) and excitation (PLE) spectra were recorded with an Edinburgh FS920 fluorescence spectrometer (Edinburgh Instruments Ltd, Livingston, UK) using a 450 W xenon arc lamp as the excitation source. Samples were put on a metallic plate with double-sided adhesive tape. The excitation wavelength was 325 nm for all three samples. The emission spectra were measured in 0.5 nm increments from 350 to 800 nm. Experiments were performed at room temperature. The obtained spectra were analyzed using OriginPro Lab software.

Diffuse reflectance (DR) analyses were performed on a UV 3600 Plus UV–VIS–NIR spectrophotometer from Shimadzu Kyoto Japan. The spectral range of analysis was from 200 to 600 nm. The baseline was realized using Spectralon as a reference. The solid sample preparation consisted of filling the 3 mm diameter microsampling cup using the appropriate funnel (praying mantis™ sampling kit, Harrick). The sample was then flattened with a microscope glass slide and then introduced into the praying mantis™. The spectra were transformed using the Kubelka–Munk function to produce a signal, normalized for comparison between samples, enabling the calculation

of the band gaps ($E_{g,\ direct}$). The details of this analysis method have been described in detail elsewhere [19].

Raman measurements were performed on a Horiba Jobin Yvon LabRam 300 spectrometer equipped with a dispersive grating (1800 gratings/mm) and equipped with an Andor iDus CCD detector (256x1064 pixels) cooled at -68 °C by a Peltier device. The spectrometer was connected to an Olympus BX40 confocal microscope and used a 532 nm DPSS Nd:YAG laser (Cobolt Samba 500). Spectra were recorded using a 50x (NA 0.5) microscope objective with an approximate power of 4 mW at the sample and an acquisition time of 30 s with a spectroscopic resolution of 3 cm^{-1}.

The zeta potential was measured on the different colloids with a DelsaNano C device from Beckman Coulter, giving information about colloidal stability.

2.3. Photocatalytic experiments

The photocatalytic performances of the different synthesized powders were evaluated by the degradation of a model pollutant, p-nitrophenol (PNP).

For this purpose, tests tubes were filled with 10 mg of the as-synthesized zinc oxide and dispersed in 10 mL of a 10^{-4} M p-nitrophenol aqueous solution continuously under stirring. They were placed at 3 cm from the halogen lamp (230W), covering a spectrum from 300 to 800 nm. The lamp and tubes were maintained at a temperature of 20 °C by a water circulation system.

In parallel, and in order to distinguish photocatalytic degradation of PNP from adsorption, duplicates of all tubes were made and placed in the dark.

The absorbance of the PNP solution was measured after 4, 8 and 24 h by withdrawing 1 mL of each PNP solution with a syringe and passing the solution through a 0.2-micron filter in order to remove the solid fraction. The filtered solution was placed in a polymethyl methacrylate (PMMA) cuvette to which 2 drops of 0.01 M HCl were added to analyze only the acidic form of the pollutant. Measurements were done by using a UV-VIS spectrophotometer (Genesys 150 UV-VIS from Thermo Scientific) at a wavelength of 317 nm, which corresponds to the absorption peak of PNP's acidic form.

3. RESULTS AND DISCUSSION

3.1 Crystallinity, Texture and Morphology

Figure 1 shows the diffractograms corresponding to the three different ZnO morphologies obtained *i.e.*, NR, ND and NF. All the diffractograms show the characteristic peaks of ZnO in its wurtzite phase located at 2θ of 31.6°, 34.3° and 36.1° without impurities. The differences in intensity of the peaks located at 31.6 and 36.1 between NR and ND highlights a preferential orientation of the (100) and (101) crystallographic planes for NR (corresponding to the non-polar facets) and (002) for ND (corresponding to the polar facets of ZnO) [20–22], as illustrated in Figures 2 and 3. In order to compare the proportion of polar *versus* non-polar facets exposed, a ratio of the areas of the three main peaks, *i.e.* the area of the second peak divided by the area of the sum of peaks 1 and 3, was calculated; the results are shown

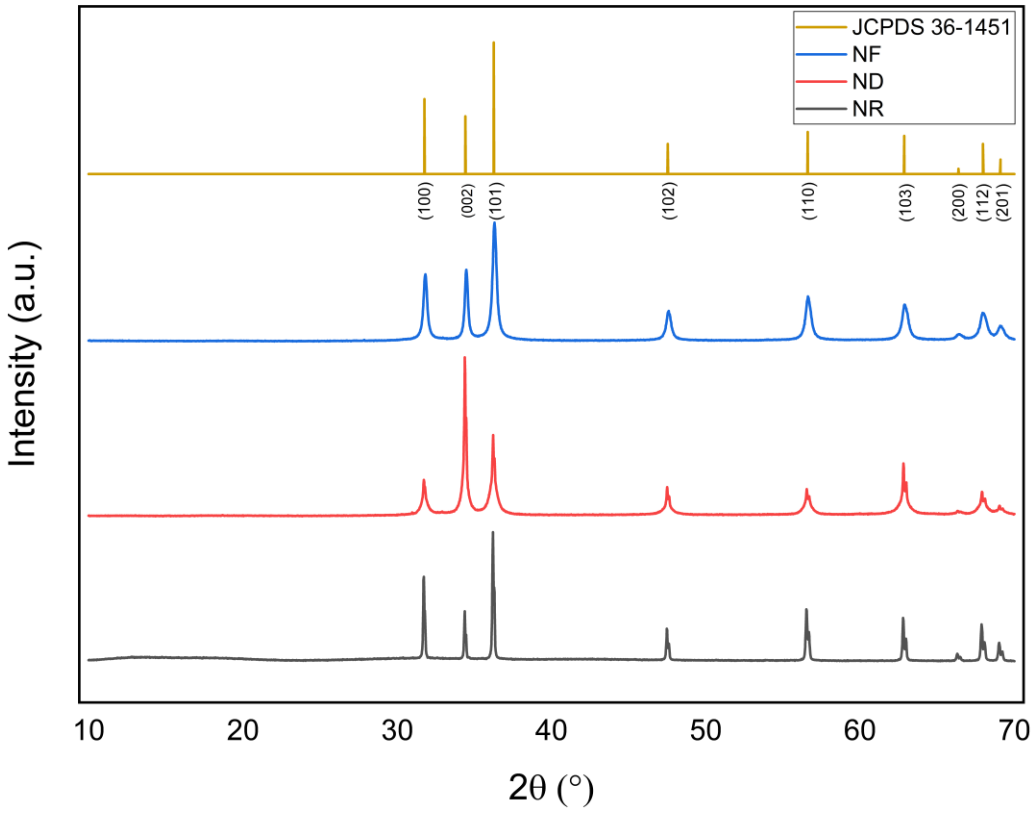

in Table 1. The intensity of the peak located at 34.3° being higher than the two other peaks (31.6° and

Figure 1. XRD pattern for the three catalysts, from the bottom to the top : NR, ND and NF and ZnO wurtzite JCPDS 36-1451

36.1°), the ND show the higher proportion of (002) facets with a ratio of 0.9 followed by the NF and then NR. For the NR, the non-polar facets are dominant, contrary to the ND where the polar facets are principally exposed [21](Figure 2).

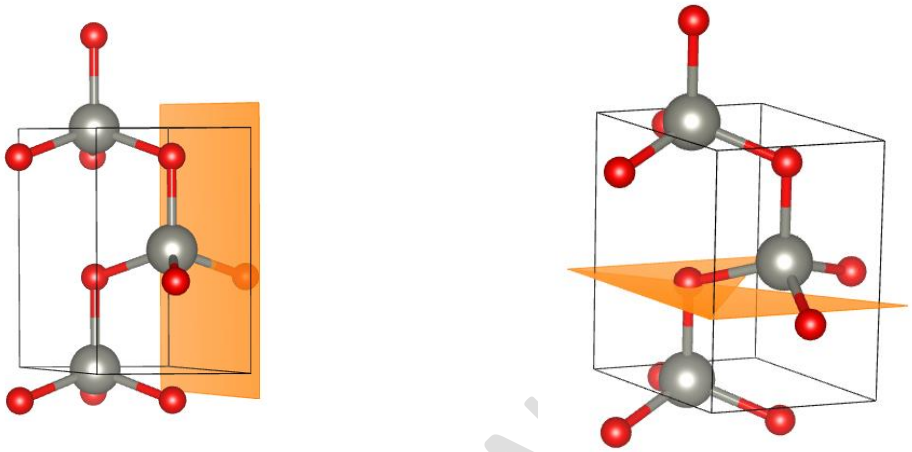

Figure 2. On the left, preferential growth along the C-axis (orange) for the NR (exposing non-polar facets) and on the right, preferential orientation perpendicular to the C-axis (orange) plane for the ND (exposing polar facets)

These preferential growths can be explained by the fact that the HMTA used in the synthesis acts as a source of hydroxide. Indeed, under the effect of temperature, HMTA decomposes into formaldehyde and ammonia. The latter reacts with water in order to form hydroxide ions which react with Zn^{2+} ions producing zinc hydroxide and then oxide, as described by the following equations [22]:

$$C_6H_{12}N_4 + H_2O \rightarrow 6CH_2O + 4NH_3 \quad (1)$$

$$NH_3 + H_2O \rightarrow NH_4^+ + OH^- \quad (2)$$

$$2OH^- + Zn^{2+} \rightarrow Zn(OH)_2 \rightarrow ZnO + H_2O \quad (3)$$

The zinc oxide is directly formed from the zinc hydroxides which constitute the nucleation points for the catalyst formation [23]. By only modifying the concentration of the precursors, as described in the materials and methods part (Section 2.1), ND or NR are obtained as can be seen in Figure 3. Consequently, different morphologies are obtained where different facets are exposed (Figure 4).

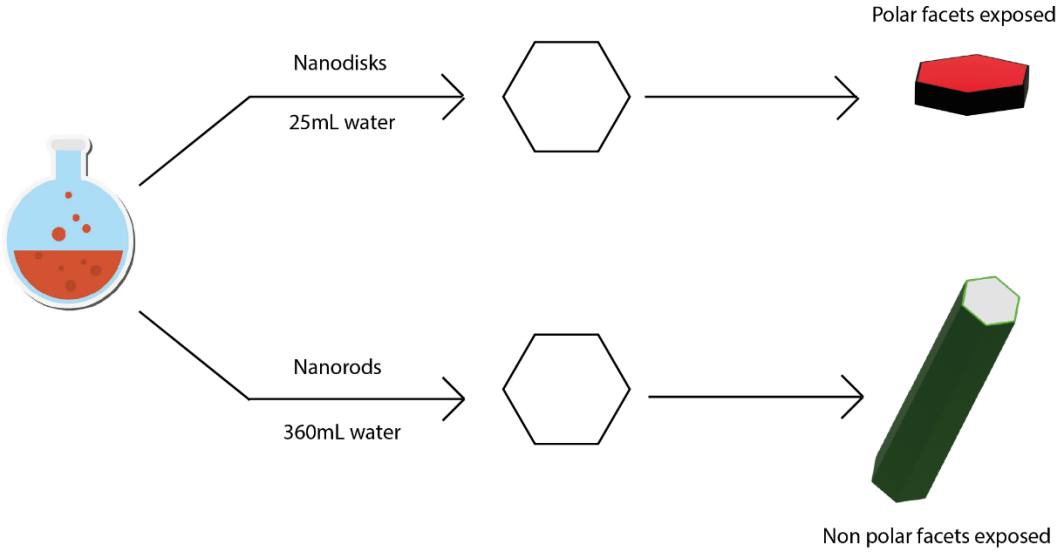

Figure 3. Synthesis of NR and ND, only the concentration of the precursors is different resulting in different morphologies.

Table 1. Data from characterization of ZnO samples: specific surface area, zeta potential, XRD, DRUVS, Raman and photoluminescence

Sample	S_{BET} (m^2/g)	Zeta pot. (mV)	XRD: A2/(A1+A3)	$E_{g,direct}$ (eV)	Raman FWHM (436cm^{-1})	Raman FWHM (97cm^{-1})	PL_Peak area 1 (PA1)	PL_Peak area 2 (PA2)	PL_Peak area 3 (PA3)	PL_(PA2/(PA_1,2,3))x100
NR	<5	-3.61	0.2	3.25	9.75	3.42	$1.19x10^6$	$1.16x10^7$	$1.25x10^6$	90%
ND	<5	3.73	0.9	3.29	13.34	3.74	$2.83x10^5$	$1.35x10^7$	$3.25x10^5$	97%
NF	10	4.57	0.3	3.29	13.88	4.56	$4.33x10^3$	$4.18x10^7$	-	99%

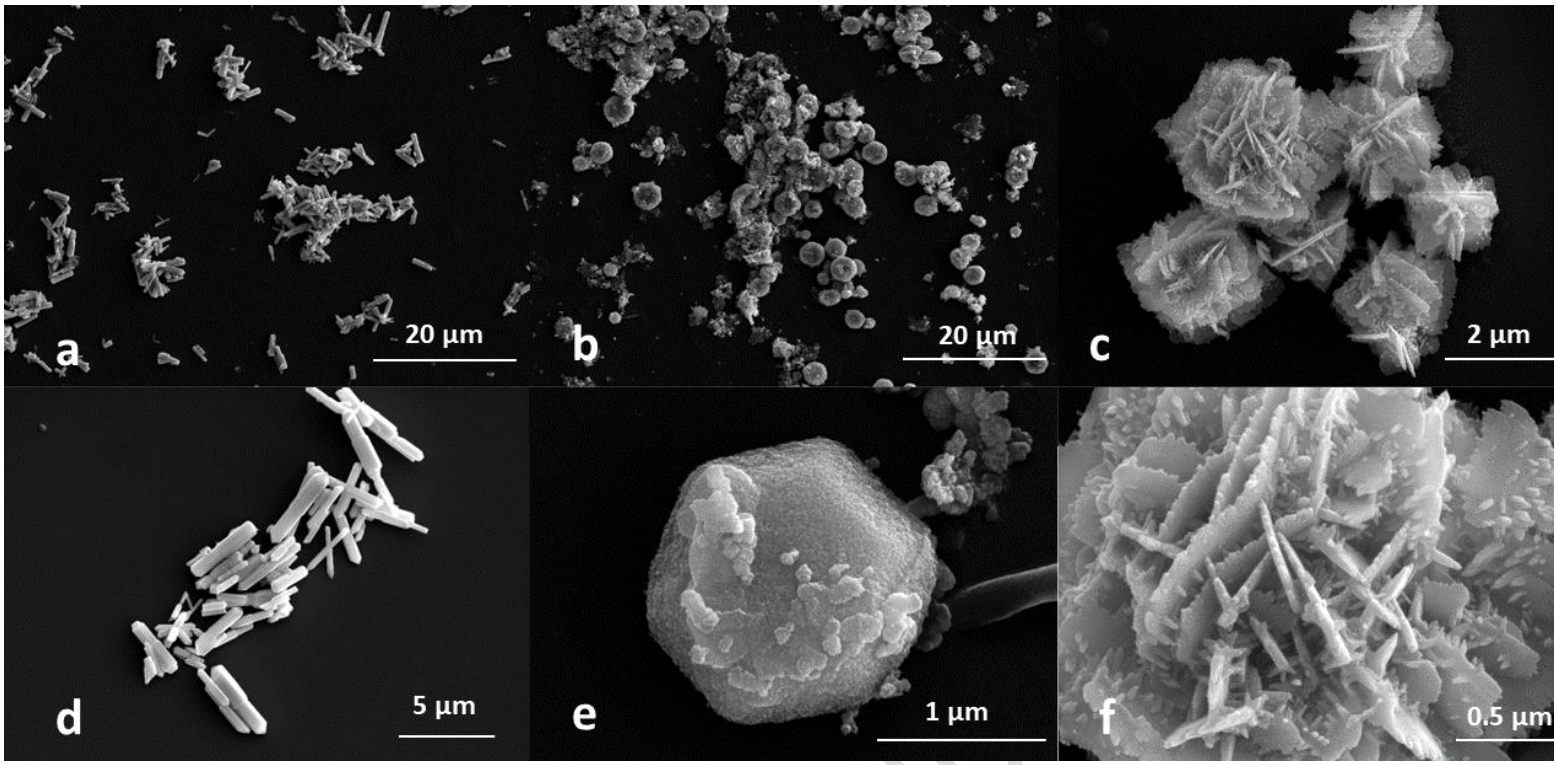

Figure 4. SEM images of the three catalysts with different magnifications. From the left to the right: NR (a) and (d), ND (b) and (e) and NF (c) and (f).

The SEM images of the three catalysts with different morphologies are shown in Figure 4. NR show preferential growth along the C-axis (Figures 4 a and d), resulting in predominantly exposed non-polar facets in contrast to ND (Figures 4 b and e) where growth occurs perpendicular to the C-axis. As the synthesis time is quite long (12 h), there seems to be some growth on the ND facets, as can be seen on Figure 4 e. Concerning NF (Figures 4 c and f), they do not seem to grow in a preferential direction, as different crystallographic planes are present but with less intensity compared to the two other powders. However, according to the intensity ratios of the XRD patterns (Table 1), the non-polar facets appear to be more exposed.

3.2 Optical properties: Photoluminescence, Raman and DRUVS

Three main peaks can be distinguished in the PL spectra (Figure 5): a peak that corresponds to the recombination of excitons around 380 nm [24]; a second broad peak in the red part of the spectrum, around 630 nm [25], that corresponds to the defects present in the crystal lattice of the zinc oxide; and, third, for the NR and ND samples, a peak in the near IR, around 750 nm [25]. By comparing the ratio between the areas under peaks 1 and 2 (Table 1), the proportion of defects present in the three different ZnO samples can be inferred. This is done in Table 1 where the ratio between the area under the second peak (PA2) and the sum of the first, second and third peaks (PA1 + PA2 + PA3) are shown, in order to estimate the defect concentration present in the crystal lattice. The NR sample is the least defective. Indeed, as it can be seen in Figure 5, the peak corresponding to the exciton recombination (380 nm), *i.e* from the conduction to the valence band is, proportionally to the peak around 630 nm, more important for the NR ZnO sample than for the two other samples. This indicates that more exciton recombination occurs in the NR compared to the ND and NF samples where many defects are therefore present, consequently decreasing the amount of recombination from the conduction to the valence band. In the literature, the nature of the defects corresponding to certain emission energies is debated and no consensus has yet been found since the mechanisms behind these transitions are not clearly understood [26]. DFT calculations have been carried out in order to calculate the energy levels of the various defects present in the crystalline structure of ZnO which gave different results [25, 27].

Nevertheless, among envisaged point defects, oxygen vacancies seem to play a significant role in the photocatalytic performance [28].

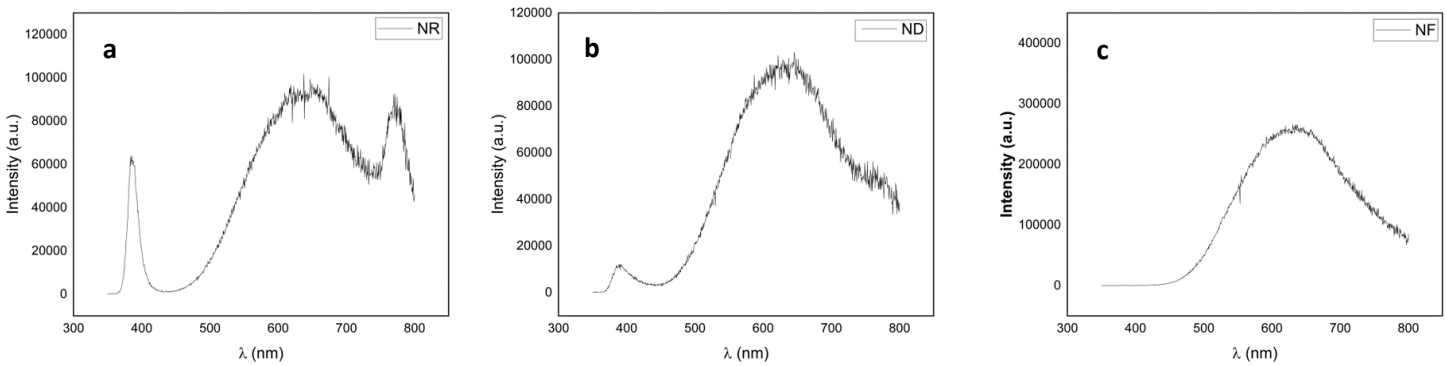

Figure 5. PL spectra (λ_{ex} = 325 nm) for the (a) NR, (b) ND and (c) NF.

In order to support the results obtained by photoluminescence, Raman spectra of the three powders were recorded (Figure 6).

As zinc oxide crystallizes in a hexagonal wurtzite structure, it is characterized by a unit cell constituted of four atoms: two zinc and two oxygen atoms (Figure 7) [29], with each zinc atom being tetrahedrally coordinated to oxygen atoms. Zinc oxide has C_{6v} point-group symmetry (or hexagonal space group P6_3mc); this group has 12 symmetry elements *i.e.*, 12 phonon modes (four atoms in the unit cell giving 3N = 12) corresponding to the irreducible representation: $\Gamma = 2A_1 + 2B_1 + 2E_1 + 2E_2$. These phonon modes split into two groups: three acoustic modes and nine optical modes. The A_1 and E_1 contributions are active in Raman and IR, the B_1 is inactive, and, finally, the E_2 modes are only active in Raman [30]. Both peaks corresponding to the E_2 modes are the most intense and represent the vibrations of zinc atoms for the peak located around 97 cm^{-1} and that of oxygen atoms for that located around 436 cm^{-1} (Figure 6). The movement of the atoms is perpendicular to the C-axis and leads to the movement of neighboring atoms, which is why this mode is called non-polar (Figure 7). The full width at half maximum (FWHM) for the peaks located at 97 cm^{-1} and 436 cm^{-1} ascend as follows: NR < ND < NF showing that the crystallinity of the NR is greater than that of ND, which is itself greater than that of

NF, highlighting the presence of a greater number of defects in the case of NF compared to ND and NR. Indeed, atoms vibrate more freely when disorder is present in the crystal lattice. This will lead to a wider peak due to the intermediate vibrational mode that can exist when defects are present, which is the case for peaks corresponding to the E_2 high mode for ZnO samples with different morphologies. Moreover, the interactions of phonons with lattice defects lead to more scattering of these phonons and thus results in a broader peak, which is the case for the E_2 high mode phonon. This is in good agreement with the peaks located between 300 and 400 cm^{-1} (shown in Figure 6 a). Indeed, these peaks are better defined for the NR than for the ND and NF, showing better crystallization. The A_1(LO) mode (Figure 6 a, blue curve) around 574 cm^{-1} is of greater intensity for NF, showing that another type of defect is more abundant in it than for the two other samples (NR and ND). This can be explained by the different synthesis method used for the NF sample compared to the two other catalysts (same synthesis with different reactant concentrations), and the absence of any thermal treatment. ~~Furthermore, the peak located at 436 cm^{-1} for NR and ND slightly shifts to higher wavenumbers for NF (437 cm^{-1}) underlining the presence of structural defects, contrary to NR and ND where only point defects are present on the surface of the catalysts.~~

All of these results are in good agreement with the photoluminescence data where the ratio between the peaks indicates the presence of more defects for the NF sample than for the two other catalysts.

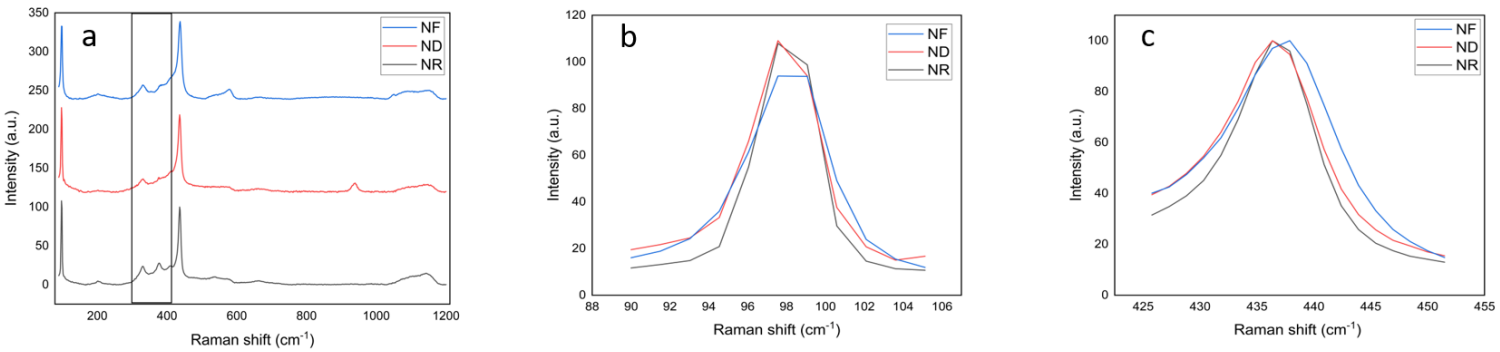

Figure 6. (a) Raman spectra for the NR, ND and NF and zoom on the two main Raman peaks located at Raman shift (b) 97cm^{-1} and (c) 436 cm^{-1}

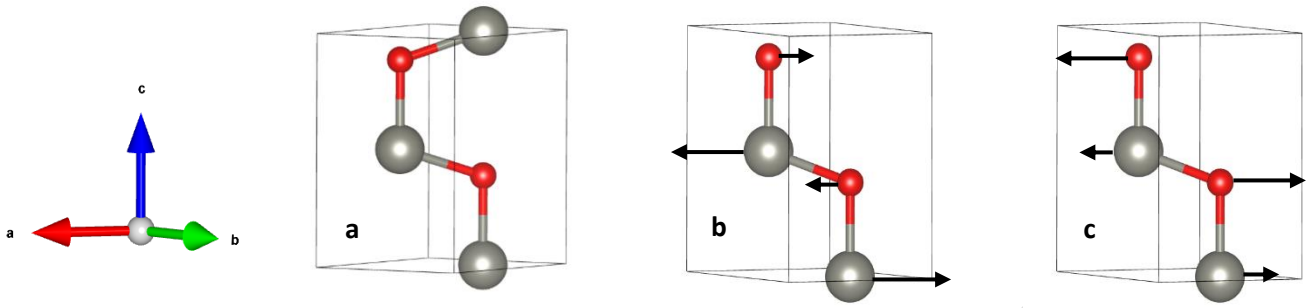

Figure 7. (a) Unit cell of the zinc oxide consisting of four atoms; (b) two zinc and two oxygen atoms in E_2 (low) vibrational mode (100 cm^{-1}) and (c) two zinc and two oxygen atoms in E_2 (high) vibrational mode (437 cm^{-1}).

The zinc oxide bandgap of the three catalysts was calculated by plotting $(F(R)hv)^2$ $(eV\ cm^{-1})^2$ as a function of the photon energy (hv). The values obtained for the ND and NF are the same (3.29 eV) but the NR show a slightly different value (3.25 eV) as can be seen in Table 1. As expected, and reported in the literature [27], similar bandgap energy values are determined from the DRUVS experiment, since all three catalysts are pure ZnO samples.

3.3 Photocatalytic activity

Figure 8 shows the PNP photocatalytic degradation under UV-vis light illumination during 24 h as obtained with the three samples. The percentage of degradation as a function of time is shown in Table 2.

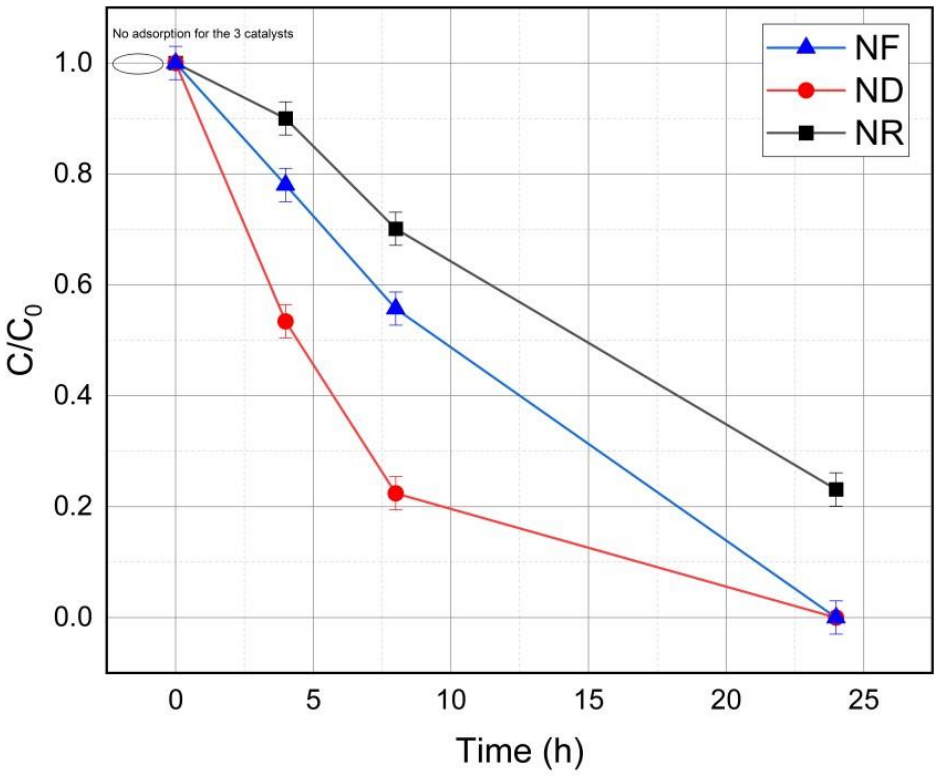

Figure 8. Degradation of PNP as a function of time for the three catalysts under halogen lamp: NR (black), ND (red) and NF (blue). Tests tubes are filled with 10mg of catalysts and 10mL of PNP 10^{-5}M.

Table 2. Percentage of degradation as a function of time for the three catalysts

Sample	PNP degradation after 4 h (%)	PNP degradation after 8 h (%)	PNP degradation after 24 h (%)
NR	10	30	75
ND	45	75	100
NF	20	45	100

First, the incident UV-vis light, which has an energy greater than the energy difference between the conduction band and the valence band ($E_{g,direct}$, Table 1) of ZnO, promotes electrons from the valence band to the conduction band, thus creating electron/hole pairs (Figure 9) [31].

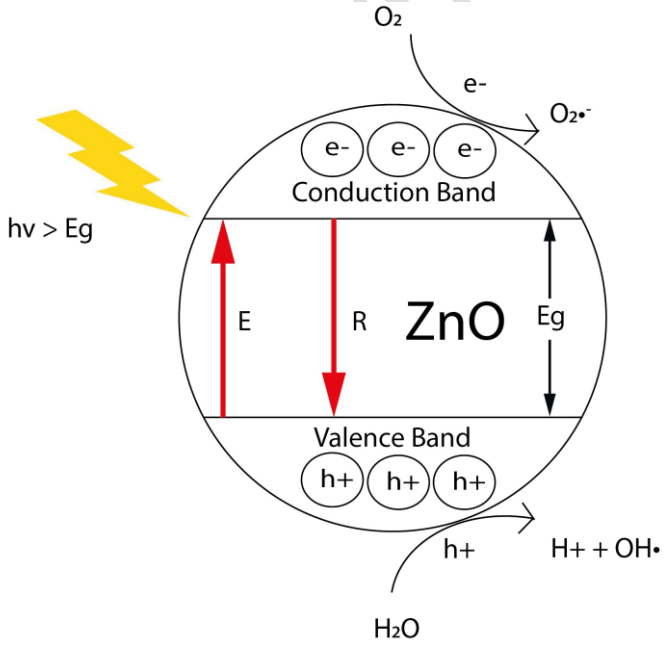

Figure 9. Mechanism for reactive oxygen species (ROS) generation under halogen lamp

These electrons and holes are involved in redox reactions creating the reactive oxygen species such as hydroxyl ($OH^{\bullet}$) and superoxide anion ($O_2^{-\bullet}$), that are involved in the PNP degradation, as described by the following equations [32]:

$$ZnO + h\nu \rightarrow e^- + h^+ \quad (4)$$

$$h^+ + H_2O \rightarrow OH\bullet + H^+ \quad (5)$$

$$e^- + O_2 \rightarrow O_2\bullet^- \quad (6)$$

$$O_2\bullet^- + H^+ \rightarrow HO_2 \quad (7)$$

$$2HO_2 \rightarrow H_2O_2 + O_2 \quad (8)$$

$$H_2O_2 + 2e^- \rightarrow 2OH^- \quad (9)$$

The degradation rates (Table 2) obtained with the three ZnO photocatalysts are as follows: NR < NF < ND. This difference can be explained by the fact that the pollutant, which is polar, interacts more easily with catalysts, especially ND, with more exposed polar facets. Indeed, the PNP molecule has an asymmetric character due to the presence of a nitro group and, in the *para* position, a hydroxyl group (Figure 10).

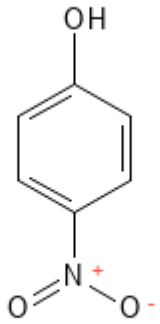

Figure 10. *p*-nitrophenol molecule

The electron-withdrawing nature of the nitro group further accentuates the polar nature of the molecule. Indeed, by attracting electrons towards it, the nitro group depletes the benzene ring of electrons, thus creating partial positive charges on the carbons of the ring compensated by the hydroxyl donor group [33]. Some of the PNP physical characteristics are summarized in Table 3.

Table 3. Physical characteristics of PNP [34].

Dipole moment (D)	**pKa**	**Solubility**
5.83	7.15	Polar solvents

From the intensity ratios of the main X-ray diffraction peaks (Table 1), it can be inferred that ND have the most exposed polar facets, followed by NF and NR. This is in good agreement with the SEM images (Figure 4). Therefore, the polar facets of ND are exposed and of two types: one Zn-ZnO terminated by zinc atoms (1010) and one O-ZnO facet (0001), terminated by oxygen atoms [35].

As the Zn-ZnO facets are positively charged, contrary to the O-ZnO facets, which are negatively charged, the distribution of these charges at short range results in the appearance of an electric dipole generating an electric field [21, 35]. When the catalyst receives sufficient light energy to create electron/hole pairs, the lifetime of these pairs is increased by the presence of the generated electric field within the catalyst [36].

In this way, this morphology promotes the interactions between the surface of the catalyst and the oxygen and water to achieve the creation of radicals that will be involved in the PNP degradation.

As the PNP molecule is itself polar, the interactions between it and the surface of the ND are much better than for NR and NF, thus allowing better adsorption of PNP on the surface of the catalyst, maximizing contacts between catalyst and pollutant and facilitating electron exchanges leading to

faster PNP degradation. NR, on the other hand, have the least polar faces, so there is less interaction between the pollutant and the catalyst resulting in a lower degradation rate.

Looking at the results obtained by the different optical techniques, NF show the highest proportion of defects, compared to NR which shows the lowest proportion of defects. Among these defects, oxygen vacancies play a determining role in the photocatalytic performance of the three catalysts [37]. Indeed, the creation of these defects involves energy states within the band gap of zinc oxide, increasing the probability of generating electron/hole pairs that contribute to the efficiency of the photocatalyst. Although NF have a higher number of defects, and a slightly better colloidal stability (Table 1) than ND, the photocatalytic activity remains lower. This shows that the exposed polar facets, with the generation of an electric field increasing the probability of electron/hole pairs generation, plays a more important role in the catalytic efficiency, by increasing the degradation kinetics obtained with the ND.

4. Conclusion

In this contribution, three zinc oxide photocatalysts were synthesized using a sol-gel process. Two catalysts were synthesized by using HMTA and zinc acetate as a precursor but in different concentrations and the third one by using zinc nitrate and NaOH. The aim of these three different syntheses was to obtain three distinct morphologies and to study their impact on the degradation kinetics of a model pollutant: *p*-nitrophenol (PNP). Three different morphologies were obtained: nanorods (NR), nanodiscs (ND) and nanoflowers (NF). The ND showed more exposed polar facets with a ratio between main diffraction peaks equal to 0.9, contrary to NR and NF where the non-polar facets are exposed (0.2 and 0.3 respectively). Moreover, the photoluminescence and Raman spectroscopy results highlighted a greater number of defects for the NF compared to the ND and the NR.

The PNP degradation efficiency is affected by several parameters such as the quantity of defects present on the surface of the catalyst and, above all, the type of exposed or non-exposed facets *i.e.* polar or non-polar. Indeed, although the NF have a higher quantity of defects, which was shown by the comparison of the ratios of the areas under the photoluminescence curves and by the FWHM of the two main Raman peaks, the morphology of the ND shows that the exposed polar facets (1010) and (0001) play a key role in the catalytic degradation reactions of PNP. The latter being respectively positively and negatively charged, and the pollutant having a non-zero dipole moment, the interactions between PNP and the ND catalyst are stronger than for the two other catalysts. In particular, the NR, for which the non-polar faces are exposed, do not allow such strong interactions with the pollutant.

The creation of radicals is facilitated by the interactions between, on the one hand, the oxygen dissolved in water and the electrons generated after illumination of ZnO and, on the other hand, the holes formed and the water molecules. It has therefore been shown that the control of the catalyst design and more particularly of the exposed polar faces is a key element for the efficiency of ZnO photocatalysts.

Acknowledgments

Julien G. Mahy and Stéphanie D. Lambert thank the F.R.S.-FNRS for their Postdoctoral Researcher position and Research Director position, respectively.

J.G.M. is also grateful to the Rotary for a District 2160 grant, to the University of Liège and the FNRS for financial support for a postdoctoral stay in INRS Centre Eau, Terre, Environnement in Québec, Canada.

The authors would like to thank the CARPOR platform of the University of Liège as well as its manager Dr. A. Léonard for the assistance in gas adsorption measurements.

Data Availability Statement

The raw/processed data required to reproduce these findings cannot be shared at this time as these data are part of an ongoing study.

Conflict of interest

The authors declare that there is no conflict of interest concerning this work.

Ethical Approval

The authors declare that they have no known competing financial interests or personal relationships that could have appeared to influence the work reported in this paper.

Consent to Participate

All authors agreed to participate in this work.

Consent to Publish

All authors agreed to this version for publication.

Authors Contributions

Antoine Farcy: Conceptualization, Methodology, Investigation, Formal analysis, Writing – original draft Writing – review & editing. Stéphanie D. Lambert: Conceptualization, Methodology, Writing – review & editing, Funding acquisition and project administration. Dirk Poelman: Investigation, Formal analysis, Writing – review & editing. Zetian Yang: Investigation, Formal analysis, Writing – review & editing Fabien Drault: Investigation, Formal analysis, Writing – review & editing. Sophie Hermans: Investigation, Formal analysis, Writing – review & editing. Patrick Drogui: Investigation, Formal analysis, Writing – review & editing. Benoît Heinrichs: Methodology, Writing – review & editing, Funding acquisition. Cédric Malherbe: Investigation, Formal analysis, Writing – review & editing. Gauthier Eppe: Investigation, Formal analysis, Writing – review & editing. Alexandre Verdin: Investigation, Formal analysis, Writing – review & editing. Julien G. Mahy: Investigation, Formal analysis, Methodology, Writing – review & editing, supervision.

Funding

For their financial support, the authors are grateful to the Ministère de la Région Wallonne Direction Générale des Technologies, de la Recherche et de l'Energie (DGO6) with support from the "31st CORNET Call" funds for the research project "DAF3D - Development of new antibacterial functionalized textiles and 3-D-printed filters for process water treatment".

References

1. Kumar Reddy DH, Lee SM (2012) Water Pollution and Treatment Technologies. J Environ Anal Toxicol 02: https://doi.org/10.4172/2161-0525.1000e103

2. Crini G, Lichtfouse E (2019) Advantages and disadvantages of techniques used for wastewater treatment. Environ Chem Lett 17:145–155

3. Dewil R, Mantzavinos D, Poulios I, Rodrigo MA (2017) New perspectives for Advanced Oxidation Processes. J Environ Manage 195:93–99

4. Mahy JG, Wolfs C, Mertes A, et al (2019) Advanced photocatalytic oxidation processes for micropollutant elimination from municipal and industrial water. J Environ Manage 250:. https://doi.org/10.1016/j.jenvman.2019.109561

5. Mahy JG, Paez CA, Carcel C, et al (2019) Porphyrin-based hybrid silica-titania as a visible-light photocatalyst. J Photochem Photobiol A Chem 373:66–76. https://doi.org/10.1016/j.jphotochem.2019.01.001

6. Nawrocki J, Kasprzyk-Hordern B (2010) The efficiency and mechanisms of catalytic ozonation. Appl Catal B 99:27–42

7. Babuponnusami A, Muthukumar K (2014) A review on Fenton and improvements to the Fenton process for wastewater treatment. J Environ Chem Eng 2:557–572

8. Lama G, Meijide J, Sanromán A, Pazos M (2022) Heterogeneous Advanced Oxidation Processes: Current Approaches for Wastewater Treatment. Catalysts 12

9. Lee KM, Lai CW, Ngai KS, Juan JC (2016) Recent developments of zinc oxide based photocatalyst in water treatment technology: A review. Water Res 88:428–448

10. Flores NM, Pal U, Galeazzi R, Sandoval A (2014) Effects of morphology, surface area, and defect content on the photocatalytic dye degradation performance of ZnO nanostructures. RSC Adv 4:41099–41110. https://doi.org/10.1039/c4ra04522j

11. Yang J, Wang J, Li X, et al (2012) Effect of polar and non-polar surfaces of ZnO nanostructures on photocatalytic properties. J Alloys Compd 528:28–33. https://doi.org/10.1016/j.jallcom.2012.02.162

12. Gan YX, Jayatissa AH, Yu Z, et al (2020) Hydrothermal Synthesis of Nanomaterials. J Nanomater 2020

13. Lai J, Niu W, Luque R, Xu G (2015) Solvothermal synthesis of metal nanocrystals and their applications. Nano Today 10:240–267

14. Kumar A, Kuang Y, Liang Z, Sun X (2020) Microwave chemistry, recent advancements, and eco-friendly microwave-assisted synthesis of nanoarchitectures and their applications: a review. Mater Today Nano 11

15. Pooyan spooyan S (2005) Sol-gel process and its application in Nanotechnology

16. Lambert S, Tran KY, Arrachart G, et al (2008) Tailor-made morphologies for Pd/SiO2 catalysts through sol-gel process with various silylated ligands. Microporous and Mesoporous Materials 115:609–617. https://doi.org/10.1016/j.micromeso.2008.03.003

17. Ward D, Ko EI, Metal Alkorides PD, Chem DC (1996) Sol-Gel Science: The Physics and Chemistry of Sol-Gel Processing. ZZZ

18. Hu J, Ding J, Ai J, et al (2021) Room temperature growth of ZnO with highly active exposed facets for photocatalytic application. Nanotechnol Rev 10:919–932. https://doi.org/10.1515/ntrev-2021-0057

19. Mahy JG, Deschamps F, Collard V, et al (2018) Acid acting as redispersing agent to form stable colloids from photoactive crystalline aqueous sol–gel TiO2 powder. J Solgel Sci Technol 87:568–583. https://doi.org/10.1007/s10971-018-4751-6

20. Luo S, Chen R, Xiang L, Wang J (2019) Hydrothermal synthesis of (001) facet highly exposed ZnO plates: A new insight into the effect of citrate. Crystals (Basel) 9:. https://doi.org/10.3390/cryst9110552

21. Wöll C (2007) The chemistry and physics of zinc oxide surfaces. Prog Surf Sci 82:55–120

22. Abubakar S, Tan ST, Liew JYC, et al (2023) Controlled Growth of Semiconducting ZnO Nanorods for Piezoelectric Energy Harvesting-Based Nanogenerators. Nanomaterials 13:1025. https://doi.org/10.3390/nano13061025

23. Wang M, Zhou Y, Zhang Y, et al (2011) From Zn(OH)2 to ZnO: A study on the mechanism of phase transformation. CrystEngComm 13:6024–6026. https://doi.org/10.1039/c1ce05502j

24. McCluskey MD, Jokela SJ (2009) Defects in ZnO. J Appl Phys 106:. https://doi.org/10.1063/1.3216464

25. Wang M, Zhou Y, Zhang Y, et al (2012) Near-infrared photoluminescence from ZnO. Appl Phys Lett 100:. https://doi.org/10.1063/1.3692584

26. McCluskey MD, Jokela SJ (2009) Defects in ZnO. J Appl Phys 106:. https://doi.org/10.1063/1.3216464

27. Janotti A, Van De Walle CG (2009) Fundamentals of zinc oxide as a semiconductor. Reports on Progress in Physics 72:. https://doi.org/10.1088/0034-4885/72/12/126501

28. Huang Y, Yu Y, Yu Y, Zhang B (2020) Oxygen Vacancy Engineering in Photocatalysis. Solar RRL 4

29. Russo V, Ghidelli M, Gondoni P, et al (2014) Multi-wavelength Raman scattering of nanostructured Al-doped zinc oxide. J Appl Phys 115:. https://doi.org/10.1063/1.4866322

30. Song Y, Zhang S, Zhang C, et al (2019) Raman spectra and microstructure of zinc oxide irradiated with swift heavy ion. Crystals (Basel) 9:. https://doi.org/10.3390/cryst9080395

31. (2016) Part 1 Fundamental Aspects of Photocatalysis

32. Azam A, Babkair SS (2014) Low-temperature growth of well-aligned zinc oxide nanorod arrays on silicon substrate and their photocatalytic application. Int J Nanomedicine 9:2109–2115. https://doi.org/10.2147/IJN.S60839

33. Vargas R, Núñez O (2009) Hydrogen bond interactions at the TiO2 surface: Their contribution to the pH dependent photo-catalytic degradation of p-nitrophenol. J Mol Catal A Chem 300:65–71. https://doi.org/10.1016/j.molcata.2008.10.029

34. Tchieno FMM, Tonle IK (2018) P-Nitrophenol determination and remediation: An overview. Rev Anal Chem 37:. https://doi.org/10.1515/revac-2017-0019

35. Chen Y, Zhao H, Liu B, Yang H (2015) Charge separation between wurtzite ZnO polar {001} surfaces and their enhanced photocatalytic activity. Appl Catal B 163:189–197. https://doi.org/10.1016/j.apcatb.2014.07.044

36. Huang M, Lian J, Si R, et al (2022) Spatial Separation of Electrons and Holes among ZnO Polar {0001} and {101¯ 0} Facets for Enhanced Photocatalytic Performance. ACS Omega 7:26844–26852. https://doi.org/10.1021/acsomega.2c03244

37. Kayaci F, Vempati S, Donmez I, et al (2014) Role of zinc interstitials and oxygen vacancies of ZnO in photocatalysis: A bottom-up approach to control defect density. Nanoscale 6:10224–10234. https://doi.org/10.1039/c4nr01887g